Computers in Biology and Medicine 207 (2026) 111645

Contents lists available at ScienceDirect

Computers in Biology and Medicine

journal homepage: www.elsevier.com/locate/compbiomed

In silico analysis of the haemodynamic disturbances caused by the subaortic membrane pathology

Alessandra Monteleone [a], Gaetano Burriesci [a,b,c,*]

[a] Ri.MED Foundation, Palermo, Italy
[b] Department of Engineering, University of Palermo, Italy
[c] UCL Mechanical Engineering, University College London, UK

ARTICLE INFO

Keywords:
Subaortic membrane
Leaflet fluttering
Subaortic stenosis
Heart valve simulation
Smoothed particle hydrodynamics (SPH)
Fluid-structure interaction (FSI)
Wall shear stress (WSS)

ABSTRACT

Subaortic stenosis, a heart disease characterised by a narrowing of the left ventricular outflow tract, is frequently caused by the presence of a subaortic membrane (SAM) located at the aortic valve inlet. This anatomical obstruction leads to significant haemodynamic alterations and leaflets fluttering, whose mechanisms are not yet fully understood. This research investigates, through computer simulations, the SAM's haemodynamic impact and the mechanism behind leaflets fluttering.

A mono-physics fluid-structure interaction approach, based on the meshless smoothed particle hydrodynamics method, was employed. This approach represents both blood and structures with particles without defining interfaces, efficiently capturing large deformations and dynamic phenomena. Two common types of SAMs were investigated - a discrete thin SAM layer (flexible) and a thick fibromuscular ridge SAM (stiff) - and compared with a healthy aortic valve.

Projected dynamic valve area (PDVA) was used as a reference parameter to quantify leaflet oscillation. While the PDVA in the healthy aortic valve stabilised at 283 mm^2 without oscillation, both pathological cases exhibited self-sustained periodic fluctuations. In the presence of discrete thin SAM layer, the mean PDVA decreased by 3% compared to the healthy control. This reduction was more pronounced for thick fibromuscular ridge configurations, where the mean PDVA was 9% lower than the healthy case. Notably, stiffer SAM configurations more than doubled the oscillation amplitude (from 3.12 mm^2 to 6.77 mm^2) and increased the oscillation frequency by 8% relative to flexible membranes. Vortices dynamics was analysed, determining the phases of their formation, growth and migration. Through the analysis of velocity, vorticity, and shear stress maps, this study provides critical insights into the origin of fluttering and its influence over these key haemodynamic parameters.

Findings demonstrate that the oscillatory leaflet motion is the result of vortices formation and shedding. The stiffness of the SAM significantly modulates the fluttering behaviour. While structural damage and haematological complications were not directly simulated, the identified oscillations represent haemodynamic conditions associated in literature with such pathologies. The observed alterations in wall shear stress magnitude and direction provide a physical basis for the mechanical environment that could contribute to endothelial cell dysfunction in the presence of SAM.

1. Introduction

Subaortic stenosis (SAS) is a cardiac disease characterised by a narrowing of the left ventricular outflow tract (LVOT) [1]. The most common subtype of SAS is the discrete subaortic stenosis (DSS), which comprises a heterogeneous spectrum of subvalvular lesions that vary in structure and mechanical behaviour. In most cases, obstruction is caused by a sub-aortic membrane (SAM), an abnormal fibrous tissue formation developing immediately beneath the aortic valve as a ring or as a crescent shape, and producing a sudden reduction of the inflow lumen [1–7]. Based on their structure, SAMs can appear as either a discrete thin fibrous diaphragm or a fibromuscular ridge formed by a thicker non-distensible membrane that can have a muscular base [2,8–14].

The prevalence of SAM in patient with congenital heart disease is 6.5% in adults [5,15], and 6% in children [16]. Moreover, it accounts for 8–30% of LVOT obstructions in the paediatric population [1,17].

* Corresponding author. Viale delle Scienze, Ed. 8 • 90128, Room 1200, Palermo, Italy.
E-mail address: gaetano.burriesci@unipa.it (G. Burriesci).

https://doi.org/10.1016/j.compbiomed.2026.111645
Received 21 January 2026; Received in revised form 18 March 2026; Accepted 20 March 2026
Available online 23 March 2026

SAM is commonly classified as a congenital disorder related to genetic factors [2,18]. However, it is also suggested that haemodynamics may play a significant role in promoting this condition [1,17,19–21]. The presence of the membrane alters the systolic blood flow from the left ventricle into the aorta and can lead to increased LVOT pressure gradient, left ventricular hypertrophy and dysfunction, aortic regurgitation, arrhythmias, and even death [1].

For the diagnosis of SAMs, echocardiography is typically used to visualise the morphology of the membrane and Doppler ultrasound is employed to measure pressure gradients [9]. The latter is a key parameter in the guidelines of the American College of Cardiology and American Heart Association for evaluating clinical treatment [22]. In this context, open-heart surgical resection of the membrane remains the only current standard of care for managing this condition. However, long-term complications and high rate of recurrence [1,7,9,23–25] have led to debates regarding the optimal timing for intervention [4,9,26].

A reported secondary complication of SAM is the fluttering of the aortic valve leaflets [27,28], a complex mechanism that is currently not fully understood. This phenomenon is also widely observed in aortic valve replacements, and known to promote calcification, haemolysis, regurgitation, accelerated fatigue and premature failure of prosthetic aortic valves [29–33]. Computational [30,34–36] and experimental [32,37–39] studies have investigated leaflet kinematic in the presence of prosthetic aortic valves. However, the mechanism by which SAM causes leaflet fluttering remains unclear and under-researched. Recently, Di Leonardo et al. [8] presented an *in vitro* analysis of the fluid dynamic changes introduced by the presence of different SAM configurations and types on a bioprosthetic aortic valve. They quantified the effect of SAM stiffness, eccentricity and obstruction grades on the aortic valve efficiency and confirmed that the presence of SAMs is associated with a substantial increase in leaflets fluttering.

In this framework, *in silico* analysis can be a powerful tool to provide a deeper understanding of this phenomenon. In particular, fluid-structure interaction (FSI) simulations, which couple computational fluid and structural dynamics (CFD and CSD, respectively) [40,41], are well-suited to model the dynamic interaction between pulsatile blood flows with highly deformable tissues (such as the heart valve leaflets and SAMs). These approaches were extensively and successfully used to study the haemodynamics of healthy and pathological heart valves [42–45].

While previous computational works investigated the impact of DSS on haemodynamics and leaflets kinematics, they were based on simplified assumptions. In this framework, Chen et al. [46] proposed a CFD analysis of the flow characteristics in the presence of different types of SAS and quantified the effects on the haemodynamics of a mechanical heart valve. However, the authors used a fixed model for the membrane and the valve components, therefore neglecting leaflet fluttering mechanisms. Guivier et al. [47] proposed a FSI study to assess the impact of subaortic stenosis in the presence of a bileaflet mechanical valve using a two-dimensional model. They found that the obstruction substantially alters leaflets kinematics, especially during the closing phase. Shar et al. [17] presented a FSI study focused on the potential implication of aortoseptal angle (AoSA) abnormalities in DSS pathogenesis. They analysed the flow and wall shear stress (WSS) characteristics in patient-specific two-dimensional left ventricle models considering a normal LVOT, an unobstructed LVOT with steep AoSA and an obstructed LVOT with steep AoSA and DSS lesion, but without including the valve leaflets. The same research group investigated the impact of AoSA steepening and DSS on aortic valve haemodynamics and regurgitation using FSI modelling [48]. While these studies offer an analysis of leaflet kinematics and discuss the formation of vortices throughout the cardiac cycle, they are limited by their two-dimensional approximation of the left ventricle and aortic valve. This simplification cannot capture the complex three-dimensional nature of blood flow patterns. The study was then extended by the same group to a three-dimensional left ventricle haemodynamic stress environment, though this analysis does not model the presence of the heart valve, thus neglecting the fluttering phenomenon [21].

This study presents the first three-dimensional computational investigation into the mechanism by which the presence of SAM leads to changes on the aortic flow and induces leaflet fluttering. To this aim, FSI simulations were performed employing the *mono-physics FSI* approach proposed by Monteleone et al. [49]. This method, previously used to simulate aortic valve haemodynamics [49] and thrombus formation [40,41], is well suited for cardiovascular applications.

The objective is to shed light on the physical origins of the fluttering phenomenon — a task that remains challenging to investigate experimentally and for which no comprehensive explanation currently exists in the literature. To this aim, an idealised modelling framework (in terms of geometry, boundary conditions, material properties and modelling assumptions) was adopted to identify the fundamental triggers of fluttering. Using an ideal healthy aortic valve model as a reference, the pathological haemodynamic alterations introduced by the SAM and their role in inducing leaflet flutter were evaluated. The impact of the common membrane types was analysed by comparing flexible and stiff configurations, representative of discrete thin layer and thick fibromuscular ridge SAMs [2,8,10,12–14], respectively.

The analysis focuses on the pathological alterations in haemodynamics leading to leaflet fluttering. Moreover, the associated WSS distributions were characterised, serving as mechanical indicators of potential endothelial cell dysfunction, as commonly adopted in the literature [36,50–52].

2. Methods

2.1. Numerical method

Computational analyses were performed using the *mono-physics FSI* approach developed by Monteleone et al. [49] and integrated into the PANORMUS (PArallel Numerical Open-souRce Model for Unsteady flow Simulations) software [53], which was demonstrated to be suited for analysis of aortic valve haemodynamics [49]. A brief overview of the method is provided below; for a more detailed explanation, refer to Ref. [49].

The approach is based on the smoothed particle hydrodynamics (SPH) method [54–57], a meshless, Lagrangian technique that employs particles to represent the computational domain. The SPH method operates through discrete convolution integrals using filter functions (known as kernel functions) defined by a characteristic smoothing length, h. This length determines the extent of each particle support domain (a local region around a particle from which it gathers information from its neighbours) and plays a role analogous to cell size in grid-based methods, directly affecting simulation resolution and accuracy.

The *mono-physics FSI* technique exploits the meshless feature of the SPH method. Specifically, SPH particles contribute to define both the fluid and structural domains within a unified physical framework, eliminating the need for separation interfaces between the two domains. Fluid and solid particles follow the same truly incompressible SPH (ISPH) numerical scheme, based on the fractional-step resolution of the governing equations. To capture structural behaviour, solid particles are interconnected through spring bounds with elastic constant providing the material Young's modulus. During each simulation step, internal elastic forces are computed to restore the spring elements to their rest lengths. These forces are then incorporated into the ISPH scheme in the predictor-step of the employed projection algorithm [40,49].

The implicit FSI coupling enables the method to efficiently handle complex phenomena such as contact interactions, large deformations and intricate geometries. It thereby addresses common limitations found in traditional FSI strategies, such as the treatment of FSI interfaces (which require accurate enforcement of matching conditions), the need for remeshing when large deformations occur and the difficulty of

accurately modelling complex dynamics (like valve coaptation during closure) [58–61].

2.2. Simulation setup

The geometry of the aortic root, valve and SAM and the specified boundary conditions are shown in Fig. 1, that provides top, lateral and isometric views of the model (panels *a*, *b*, and *c*, respectively). The aortic root and valve models are based on the works of Tango et al. [42,62]. Specifically, the valve leaflets are obtained from the idealised healthy human aortic valve model described by Thubrikar [63]. These were pre-expanded to a semi-opened position used as starting configuration for the simulations (see Fig. 1a). The model features a 25 mm diameter for both the *aortic annulus* and the *sino-tubular junction* (see Fig. 1b), as described in Swanson and Clark [64]. The Valsalva sinuses, which are three pouches at the base of the aortic root hosting each of the leaflets during valve opening, are assumed to be identical. Their shape is defined by an epitrochoid, as described in Reul et al. [65], with a maximum cross-section circumscribed to the aortic nominal diameter of 25 mm and inscribed within a 36.44 mm diameter circle. The SAM, comprised between dashed red lines in Fig. 1a and represented as red regions in Fig. 1b and c, is modelled as a membrane with a circular hole concentric to the aortic valve axis, with *membrane orifice area* (MOA) equal to 50% of the unobstructed inflow lumen at the *annulus* section. It is placed 8 mm upstream from the leaflet base (see Fig. 1b), which is consistent with the typical mean distance [8,66].

In this work, two common types of SAMs were investigated and compared with a healthy aortic valve (AV).

In particular, the following scenarios were analysed:

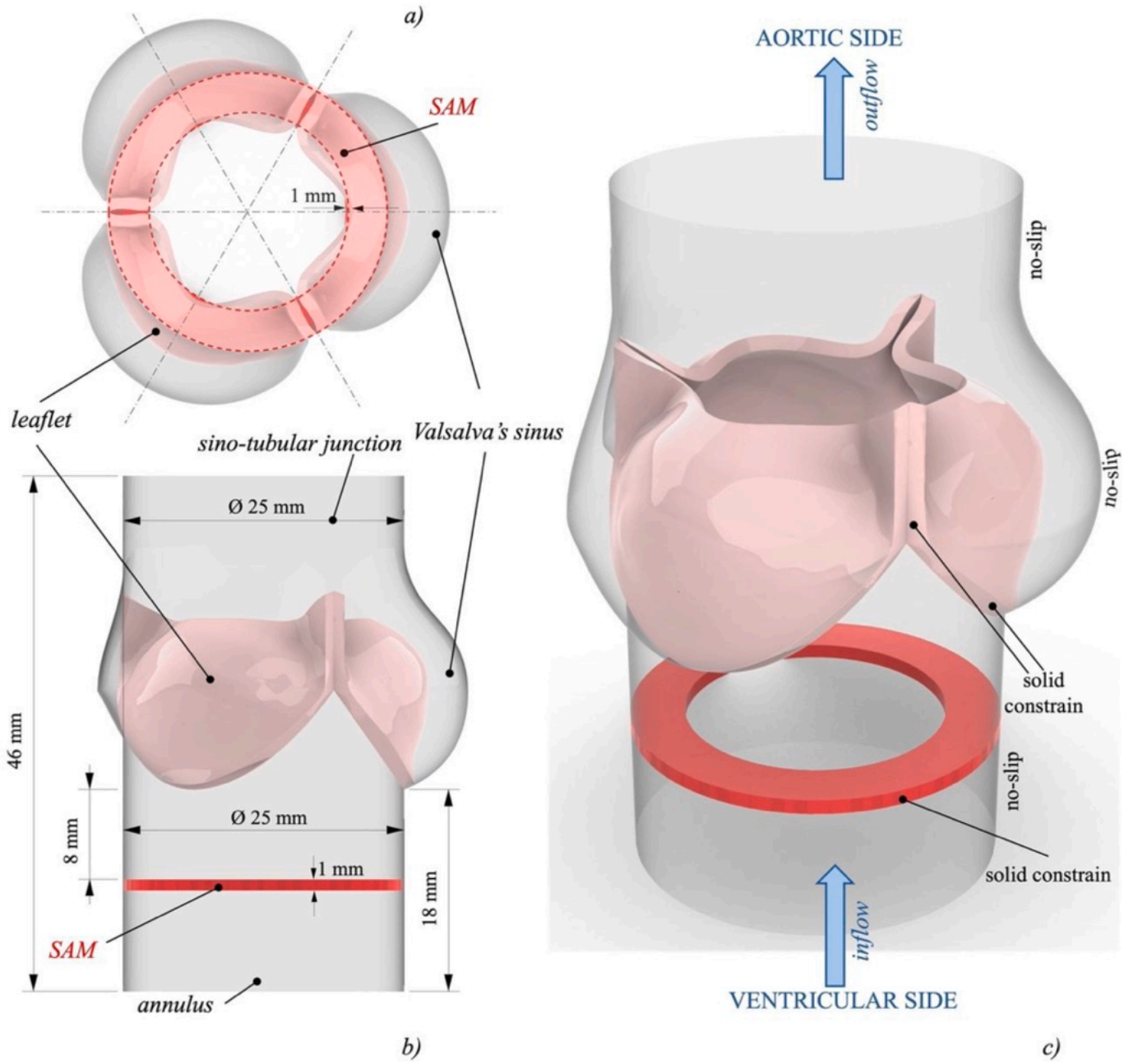

Fig. 1. Geometric model for FSI numerical simulations. a) Top view; b) lateral view; c) 3D visualisation with the indication of the boundary conditions for the fluid and solid domains.

- *Healthy AV*: This model represents an aortic valve without the SAM, thus representative of the healthy case used as reference for the study. Therefore, the red region in Fig. 1 is not included in this configuration;
- *Flexible SAM*: This model represents a discrete thin SAM layer which consists of a highly flexible thin fibrous diaphragm [8,12–14]. The SAM was modelled with the same material properties as the valve leaflets;
- *Stiff SAM*: This model simulates a thicker fibromuscular ridge SAM, which presents as a robust ring of tissue, causing a less deformable narrowing of the LVOT [8,12–14]. The same geometry of the *flexible SAM* was employed (see Fig. 1); however, to achieve a stiffer membrane, the Young's modulus of the SAM was set to ten times that of the valve leaflets.

Boundary conditions for fluid and structural domains are detailed in panel *c* of Fig. 1. The aortic root walls were modelled as rigid, imposing no-slip boundary conditions. It should be noted that this study focuses on the ejection phase of the aortic valve; therefore, only the ejection phase was considered, as the diastolic phase is inconsequential to the fluttering mechanism [8,35]. Specifically, starting from a semi-opened configuration (see Fig. 1), a constant pressure difference between the ventricular and aortic sides was imposed, with an initial linear ramp, until the mean blood velocity stabilised. To this end, pressure conditions were applied at the inflow and outflow sections following the open-boundary procedure proposed by Monteleone et al. [67]. In the *healthy AV* case, a pressure difference of 3.5 mmHg (after the initial linear ramp) yielded a mean blood velocity of 0.6 m/s. This velocity is consistent with typical physiological systolic flows [68]. The pressure gradient was increased in the *flexible* and *stiff SAM* simulations (by 7% and 12%, respectively) to achieve the same mean velocity as in the healthy configuration. Notably, although the prescribed pressure difference was held constant to achieve a steady mean blood velocity, the resulting fluid-structure interaction analysis remains inherently transient due to the leaflet fluttering phenomenon.

Leaflets and membrane were fully constrained at their regions contacting the aortic root and LVOT, respectively, as shown in Fig. 1c.

Blood was modelled as an incompressible Newtonian fluid, with dynamic viscosity, μ, of 0.0035 Pa · s and density, ρ_f of 1060 kg/m^3. Density of solid tissues was imposed equal to that of the fluid ($\rho_f = \rho_s$).

As the pressure acting on the aortic root is maintained constant throughout the analysed period, no significant effects associated with root compliance are expected. Hence, the use of a non-deformable root was preferred to ensure consistent anatomical configurations across all models, independently of the applied pressure conditions, thereby facilitating direct comparison of the observed mechanisms.

Leaflets are modelled as linear elastic material, simplifying their non-linear and anisotropic properties [69–72]. A Young's modulus $E_{leaflet} = 50$ kPa was selected for the leaflets, providing similar response to that measured for leaflets material under low strain, which characterises the valve opening phase [45,73,74].

In the *flexible SAM* and *stiff SAM* simulations, the same linear elastic model is used with different stiffness values to represent the two membrane types: $E_{Flexible\ SAM}$ equal to 50 kPa and $E_{Stiff\ SAM}$ equal to 500 kPa.

Table 1 summarises the material properties used for the blood and structures and the pressure difference between inflow and outflow sections used in the simulations.

The root inner volume was discretised with a smoothing length of 325 μm, as recommended in Ref. [49], resulting in a total number of 767,870 particles. Leaflets and SAMs were modelled with a thickness of about 1 mm employing three layers of particles. A time step of 0.025 ms (for a total of 13,200 iterations) was used in all simulations.

Table 1
Material properties and pressure conditions.

Parameter	Value
Fluid density (ρ_f)	1060 kg/m^3
Dynamic viscosity (μ)	0.0035 Pa · s
Pressure difference between the ventricular and aortic sides	*Healthy AV* simulation: 3.5 mmHg *Flexible SAM* simulation: 3.745 mmHg *Stiff SAM* simulation: 3.92 mmHg
Structure density (ρ_s)	1060 kg/m^3
Young's modulus of structures ($E_{leaflets}$)	50 kPa
Young's modulus of *Flexible SAM* ($E_{Flexible\ SAM}$)	50 kPa
Young's modulus of *Stiff SAM* ($E_{Stiff\ SAM}$)	500 kPa

2.3. PDVA identification

In order to evaluate and quantify the leaflet fluttering phenomenon, the projected dynamic valve area (PDVA) was considered. This parameter is a measure of the valve instantaneous opening area, calculated by projecting the space enclosed by the leaflets onto a plane perpendicular to the valve axis [8,30,34,75]. PDVA is widely used to approximate the geometric orifice area, although it actually represents the envelope of the GOA at the different cross sections within the valve area.

Fig. 2 shows a sketch describing the calculation procedure of the PDVA parameter. Specifically, the method involves dividing each leaflet into nine equally spaced sections (Fig. 2a). For each section, the closest particle on the leaflet inner surface is identified (see particle A in Fig. 2a). The coordinates of this particle are then projected onto a plane perpendicular to the valve axis (see the projection of A on the plane π, point A′, in Fig. 2b), and the distance from this projected point to the centre of the valve annulus is measured ($r_{A'}$ in Fig. 2b). After repeating the process for all the twenty-seven sections, the average of these distances is calculated to obtain a mean radius, which is then used to compute the area at that specific moment in time. This entire procedure is performed for each time instant to obtain a dynamic measurement.

3. Results

Fig. 3a shows the evolution of the PDVA for the three simulated scenarios: *healthy AV* (continuous black line), *flexible SAM* (dotted black line) and *stiff SAM* (dashed black line). In the *healthy AV* case, two smooth oscillations are observable at the beginning of the opening phase, with fluctuation peaks at 0.023 s and 0.075 s. After this initial phase, the PDVA rises to a stable value of approximately 283 mm^2, without any further oscillations being detected. The PDVA measured in the *flexible SAM* simulation presents an initial smooth oscillation at 0.03 s, followed by a small oscillation at 0.115 s. The PDVA then enters a phase of self-sustained oscillations with a mean value of about 275 mm^2. For the *stiff SAM* (dotted black line), up to 0.1 s the PDVA curve is practically superposed to that of the *flexible SAM*, but then starts fluctuating with larger oscillations around a mean value of approximately 257 mm^2.

The PDVA curves of the *flexible* and *stiff SAM* were fitted with a third-order Fourier series using the *Curve Fitter Tool* in MATLAB R2024b and the fundamental frequency with its amplitude (defined as the distance from midline to the crest) was considered for the analysis. Fig. 3b shows the fit for the *flexible SAM* (dotted red line) and *stiff SAM* (dashed red line) after the PDVA oscillations has stabilised. In the *flexible SAM* case, the oscillation frequency was equal to 27.5 Hz, with amplitude of 3.12 mm^2. In contrast, the *stiff SAM* case exhibited an oscillation frequency of 29.7 Hz and a significantly larger amplitude of 6.77 mm^2.

Fig. 4 provides, for the three simulated scenarios, a three-dimensional visualisation of the velocity field at the time of maximum PDVA. The instant of maximum PDVA depends on the considered

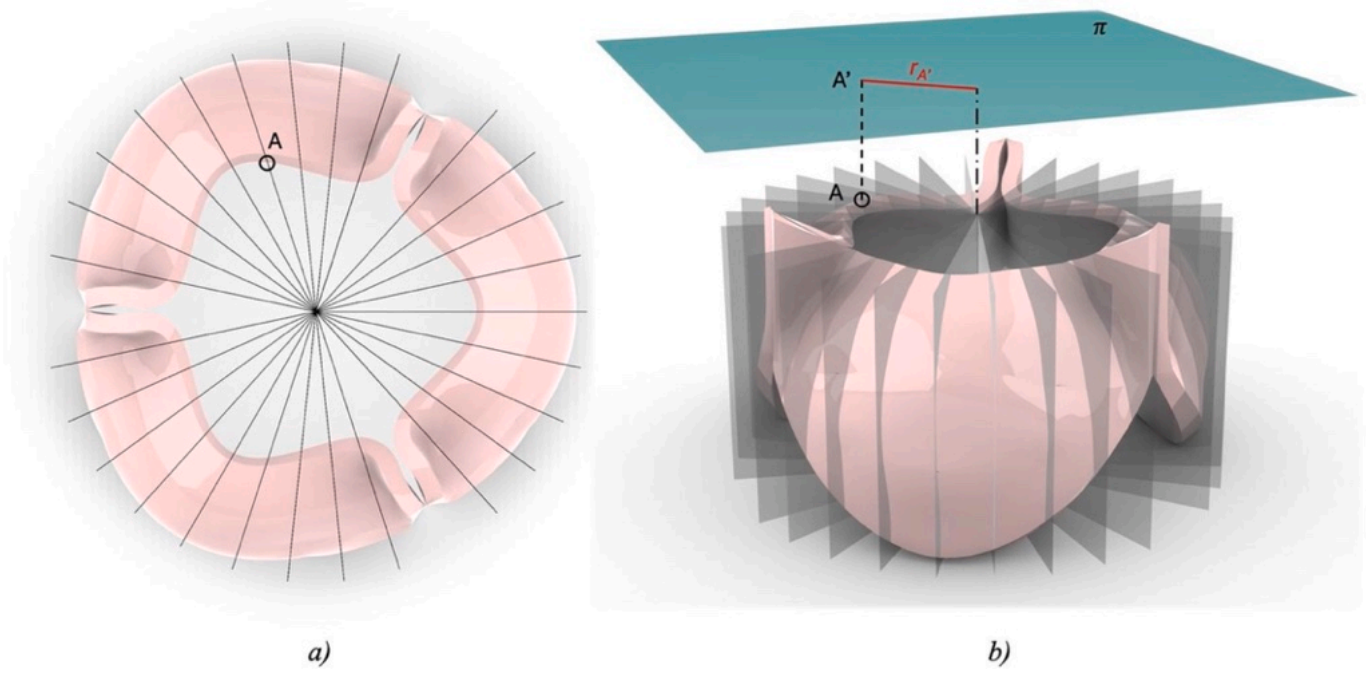

Fig. 2. Determination of the projected dynamics valve area (PDVA). a) top view; b) perspective view.

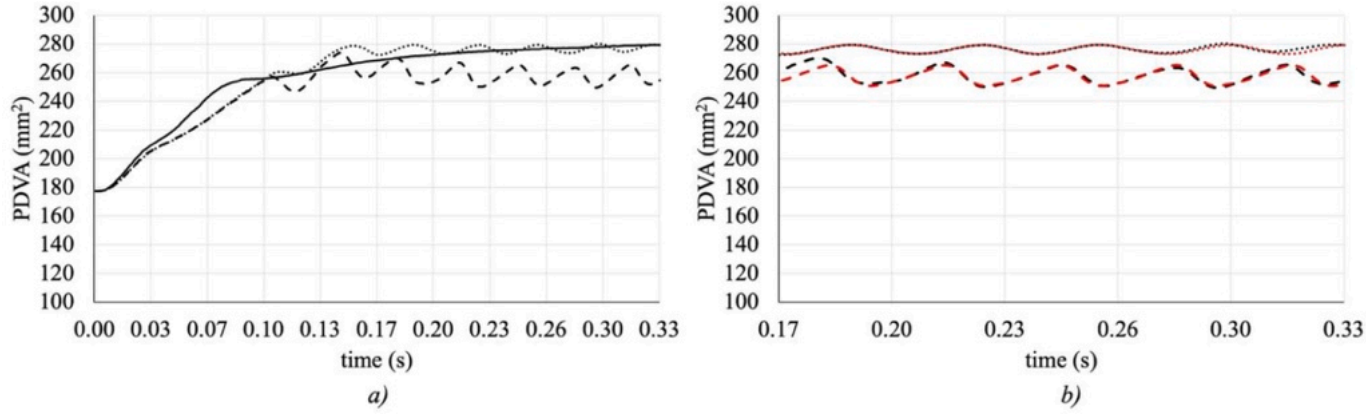

Fig. 3. a) PDVA evolution over time for the healthy AV (continuous black line), flexible SAM (dotted black line) and stiff SAM (dashed black line); b) fitting with the Fourier series for flexible SAM (dotted red line) and stiff SAM (dasThe following are the Supplementary data related to this article: hed red line). (For interpretation of the references to colour in this figure legend, the reader is referred to the Web version of this article.)

scenario. In the *healthy AV* model, no oscillatory behaviour was observed, and the instant at time 0.30 s, when PDVA had already reached stabilisation, was considered. In the presence of the membrane, PDVA oscillates cyclically, therefore, a positive peak of the oscillation was considered. Specifically, the peaks at 0.225 s and 0.248 s were selected for the *flexible* and *stiff SAMs*, respectively. The deformed configurations of the leaflets and membranes are represented with white dots. A video showing the velocity field during one oscillation cycle is provided for the *stiff SAM* case as Supplementary Content (Video S1).

Supplementary data related to this article can be found online at https://doi.org/10.1016/j.compbiomed.2026.111645

In Fig. 5, the velocity and streamlines, vorticity maps and fluid shear stress distribution are represented for the three analysed scenarios, at the instant of maximum PDVA, on a longitudinal plane of symmetry. The velocity and streamlines (in Fig. 5a) are represented using line integral convolution (LIC), which gives an immediate visualisation of vortices forming during ejection. The vorticity maps (Fig. 5b) provide a quantification of the rotational intensity of the fluid. The shear stress distribution (Fig. 5c) is another useful parameter, as it is associated with the blood damage potential of the system.

Figs. 6 and 7 show the velocity streamlines for the *flexible* and *stiff SAMs*, respectively. These figures illustrate four key instants within a single PDVA oscillation cycle: the trough corresponding to minimum PDVA (time t_1); the midline crossing during ascent (time t_2); the peak corresponding to maximum PDVA (time t_3); the midline crossing during descent (time t_4). To highlight the vortices that drive leaflet oscillations, they are drawn and labelled with capital letters (*A*, *B* and *C*). Vortices generated in the preceding PDVA oscillation cycle are indicated with the subscript '*ex*'.

For the direction of vortical rotations, the convention proposed in Ref. [68] is adopted, where a vortex following the ejected flow close to the root axis and opposite direction close to the arterial wall is denoted as positive, while a vortex with opposite rotation is denoted as negative. The vortex sign is indicated using superscript '+' for positive and '−' for negative.

A video showing the velocity streamlines during one oscillation cycle

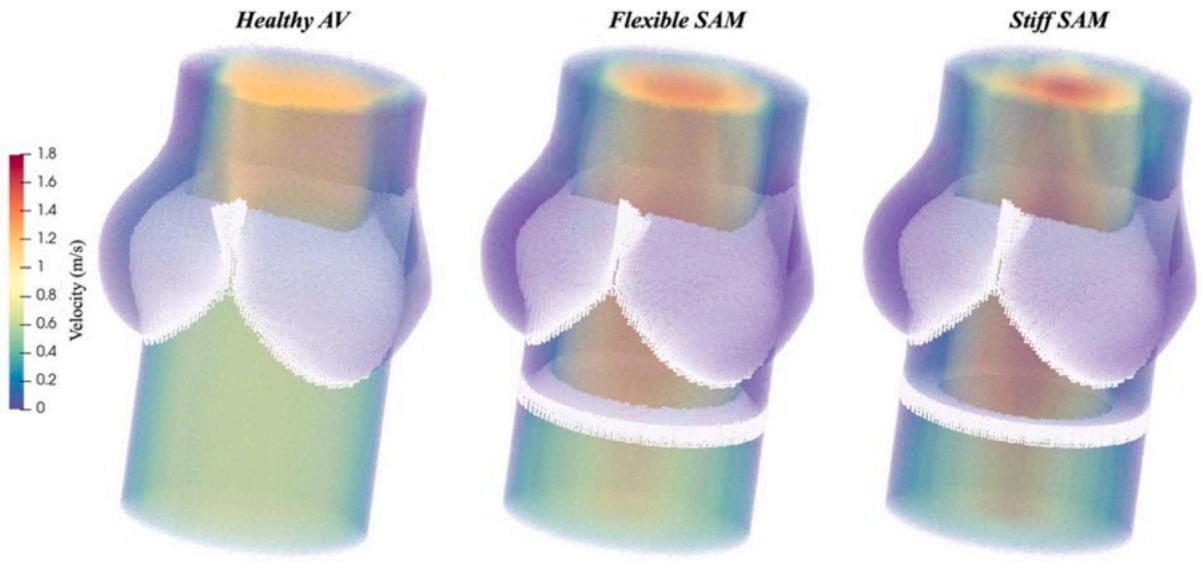

Fig. 4. 3D visualisation of the velocity field at a maximum PDVA (0.225 s and 0.248 s for the flexible and stiff SAM cases, respectively. In the healthy AV, PDVA does not oscillate, therefore, the stabilised configuration at 0.3 s is shown). Leaflets and membranes are represented with white dots.

and the leaflet fluttering is provided for the *stiff SAM* case as Supplementary Content (Video S2).

Supplementary data related to this article can be found online at https://doi.org/10.1016/j.compbiomed.2026.111645

Fig. 8 shows the velocity component normal to the leaflet surface for the *stiff SAM* case. Although the underlying mechanism is the same as in the *flexible SAM* configuration, the *stiff SAM* is shown because it produces velocity magnitudes approximately 50% higher. Velocity fields are reported at the four characteristic instants of the fluttering cycle (t_1–t_4) and at intermediate instants.

Leaflet dynamics are governed by alternating expanding (red) and contracting (blue) waves that propagate cyclically from the leaflet inflow region toward the free edge. At t_1 (minimum PDVA), an expanding front originates at the bases of the right and left *lunulae* (the thickened, crescent-shaped regions of the cusps) and converges at the *nodulus of Arantius*. By t_2 (PDVA inflection), this positive front spans the entire free edge, while a contracting front with the same spatial footprint begins to form. This negative wave propagates toward the free edge (t_3), reaching it at t_4, where a new expanding front is already emerging at the *lunulae* bases.

Fig. 9 shows the WSS magnitude and vector fields on both the ventricular and aortic sides of a representative leaflet for the three scenarios considered. In the *healthy AV* (Fig. 9a), WSS vectors exhibit a coherent and predominantly axial orientation on both surfaces. In contrast, the pathological configurations (*flexible* and *stiff SAM*) display markedly disordered WSS vector patterns and spatial heterogeneity throughout the oscillation cycle, as evident at the characteristic instants t_1–t_4 in Fig. 9b and c. These haemodynamic derangements are most pronounced on the aortic surface, where WSS magnitudes remain significantly lower than those of the healthy control across all analysed instants.

4. Discussion

Discrete subaortic stenosis pathology was computationally investigated, focusing on the flutter mechanism affecting aortic valve leaflets. In addition, the alterations in WSS magnitude and direction, recognised mechanical indicators of potential endothelial cell dysfunction [36, 50–52] were computed to evaluate the potential implications of fluttering on valvular tissue injury.

To this aim, healthy and diseased aortic valves were analysed and compared during opening. In the pathological scenario, two common types of DSS were simulated, encompassing a discrete thin SAM layer and a thick fibromuscular ridge SAM (named flexible and stiff SAMs, respectively, following the notation in Ref. [8]), both leading to an obstruction of 50% of the inflow lumen, for the unloaded configuration.

The aortic valve performance during ejection was evaluated for the three scenarios in terms of PDVA (see Fig. 3). In the *healthy AV*, after two small oscillations in the early opening phase, the PDVA rapidly stabilises at 283 mm^2 and remains steady without further fluctuations.

In contrast, both pathological cases exhibit a markedly different behaviour, with the PDVA exhibiting a small initial oscillation followed by a linear increase, after which self-sustained periodic oscillations develop. In the *stiff SAM* configuration, the oscillation frequency is slightly higher (+8% relative to the *flexible SAM*), whereas the amplitude more than doubles (6.77 mm^2 against 3.12 mm^2). This trend is consistent with findings of Di Leonardo et al. [8], who also reported higher frequency and amplitude in the stiffer membrane, although a direct quantitative comparison is not appropriate due to differences in valve configuration (a stented bioprosthesis in Di Leonardo et al. [8]), annulus dimension and material properties. Furthermore, the oscillation frequencies observed in the models lie within the range reported for bioprosthetic aortic valves with similar annulus diameter [30,35].

It should be noted that several assumptions were made to isolate the fundamental physical mechanism responsible for leaflet fluttering, avoiding any secondary effect of turbulence, patient-specific morphology and dynamic effects. To this aim, the flow was modelled as laminar and idealised geometries were used for the aortic root, valve leaflets and membrane. Moreover, the imposed boundary conditions are highly idealised, allowing to analyse only the valve open phase. In fact, preliminary analyses (not reported here) showed that, when imposing a physiological velocity waveform, the leaflet oscillations phenomenon occurs after the valve has fully opened and it is not influenced by the opening and closing dynamics of the valve. This result is further supported by the experimental findings of Di Leonardo et al. [8], who observed that the fluttering phenomenon is absent during the dynamic opening and closing phases. Consequently, their analysis focused exclusively on the stable systolic window (excluding the first and final thirds of the cycle) to accurately quantify leaflet oscillations. In light of these considerations, in this study the prescribed pressure difference between the ventricular and aortic sides is imposed constant (except for an initial ramp) and does not follow a physiological waveform (as described in section 2.2). This methodological choice allows to establish a repeatable and controlled environment which isolates the minimal physical conditions under which leaflet fluttering arises, thereby

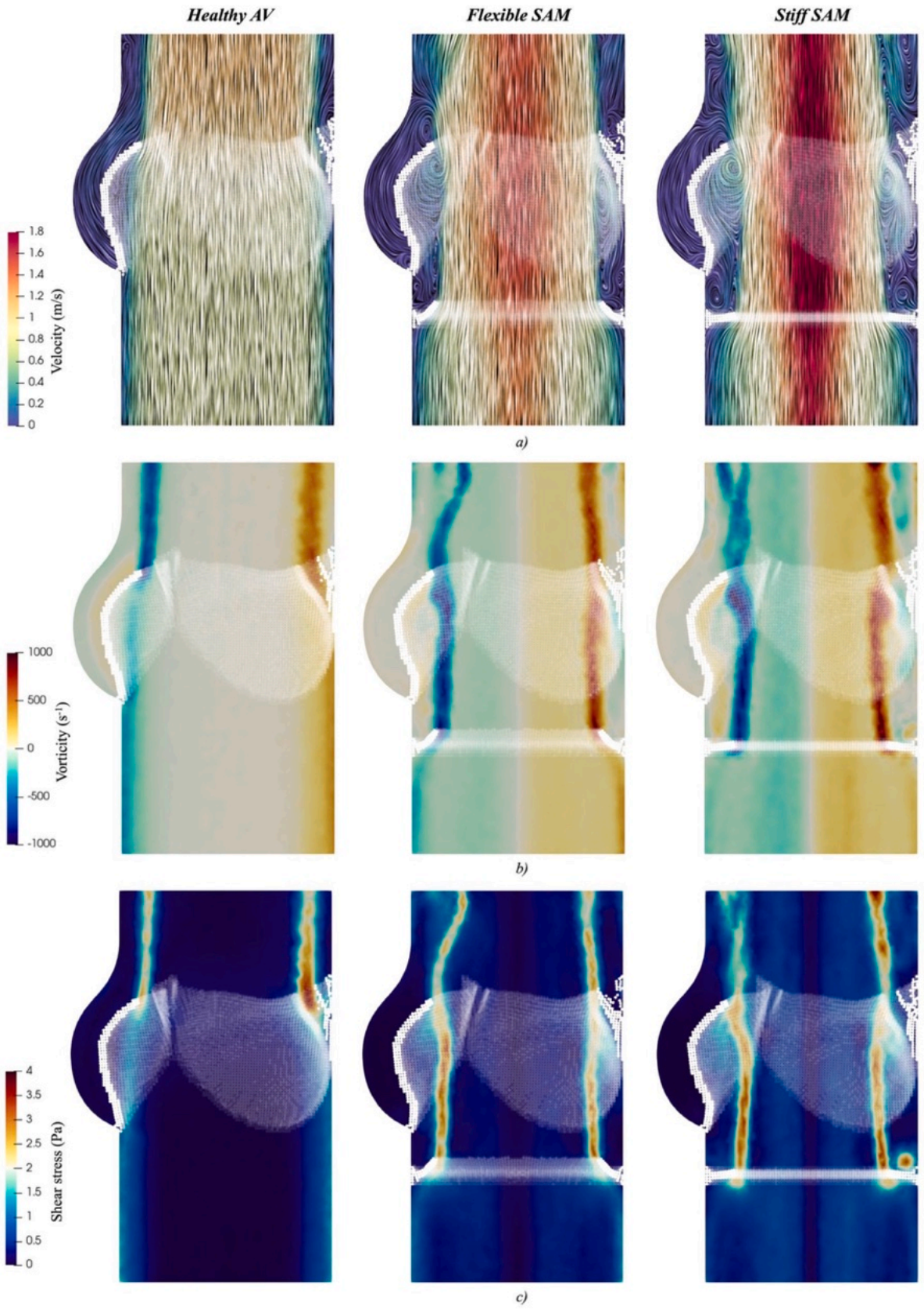

Fig. 5. Continuous maps in a longitudinal cross-section at the maximum (0.225 s and 0.248 s for the flexible and stiff SAM cases, respectively. In the healthy AV, PDVA does not oscillate, therefore, the stabilised configuration at 0.3 s is shown). Leaflets and membranes are represented with white dots. a) Velocity and LIC; b) vorticity; c) shear stress.

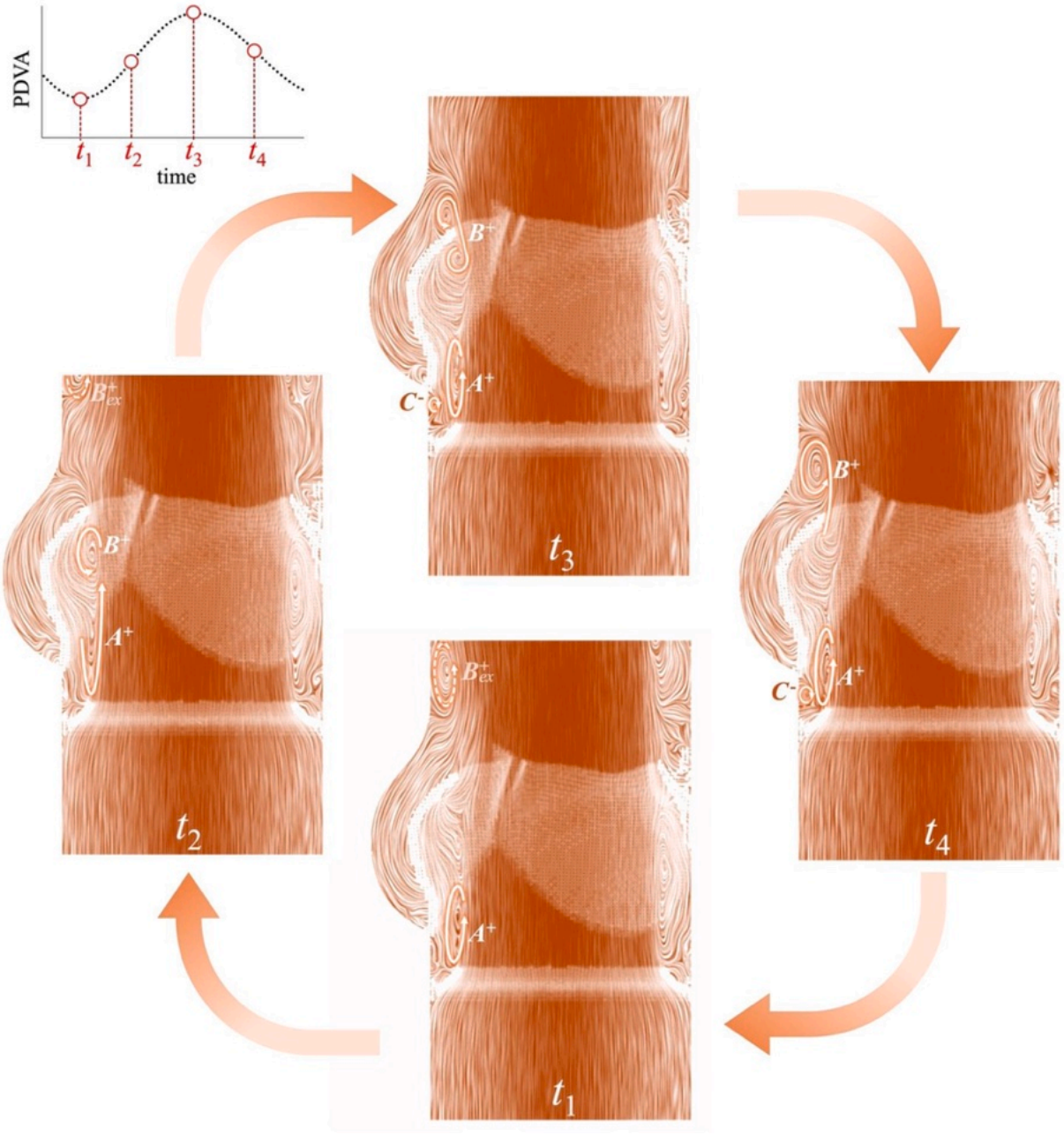

Fig. 6. Flexible SAM - velocity streamlines in a longitudinal cross-section at four characteristic instants of the fluttering cycle: t_1-trough corresponding to minimum PDVA (0.207 s); t_2-midline crossing during ascent (0.216 s); t_3-peak corresponding to maximum PDVA (0.225 s); t_4-midline crossing during descent (0.233 s).

identifying a necessary mechanism that must also be present, although potentially modulated, in more realistic settings. Under all these hypotheses, it is possible to conclude that introducing a membrane is sufficient to trigger the leaflets fluttering, which is thus entirely attributable to fluid-dynamic shedding phenomena, not to turbulence or dynamic effects.

Pathological valves exhibit a restricted opening compared with the *healthy AV*. In the presence of *flexible SAM*, the mean PDVA decreases to 275 mm^2 (≈3% lower than for the *healthy AV*), and this effect is amplified in the *stiff SAM* configuration, where the mean PDVA further drops to 257 mm^2 (9% lower than for the *healthy AV*). These results are consistent with the *in vitro* measurement reported by Di Leonardo et al. [8], who observed an increase in the oscillation amplitude and a reduced mean PDVA in the *stiff SAM* condition. The reduction in valve opening area in the presence of discrete subaortic stenosis is also well documented in clinical observations [27].

The reduced opening area impairs normal blood flow, as shown by comparison of the three-dimensional velocity fields across the three scenarios Fig. 4. This figure depicts the instant of maximum PDVA for the *SAM* models. The *healthy AV* exhibits a more uniform velocity distribution than the pathological cases, where the velocity magnitude of the ejected flow is significantly more focused at centre of the cross section, with greater effect for the *stiff SAM* case.

The three configurations lead to markedly different blood flow patterns, as highlighted in Fig. 5a, where the velocity map and streamlines at the instant of maximum PDVA are reported in a longitudinal cross-section. In the *healthy AV*, streamlines are smooth and orderly, and vortices are practically absent. In the real operating function, the *healthy AV* experiences highly pulsatile flow conditions which induce opening and closing and are accompanied by the formation and evolution of

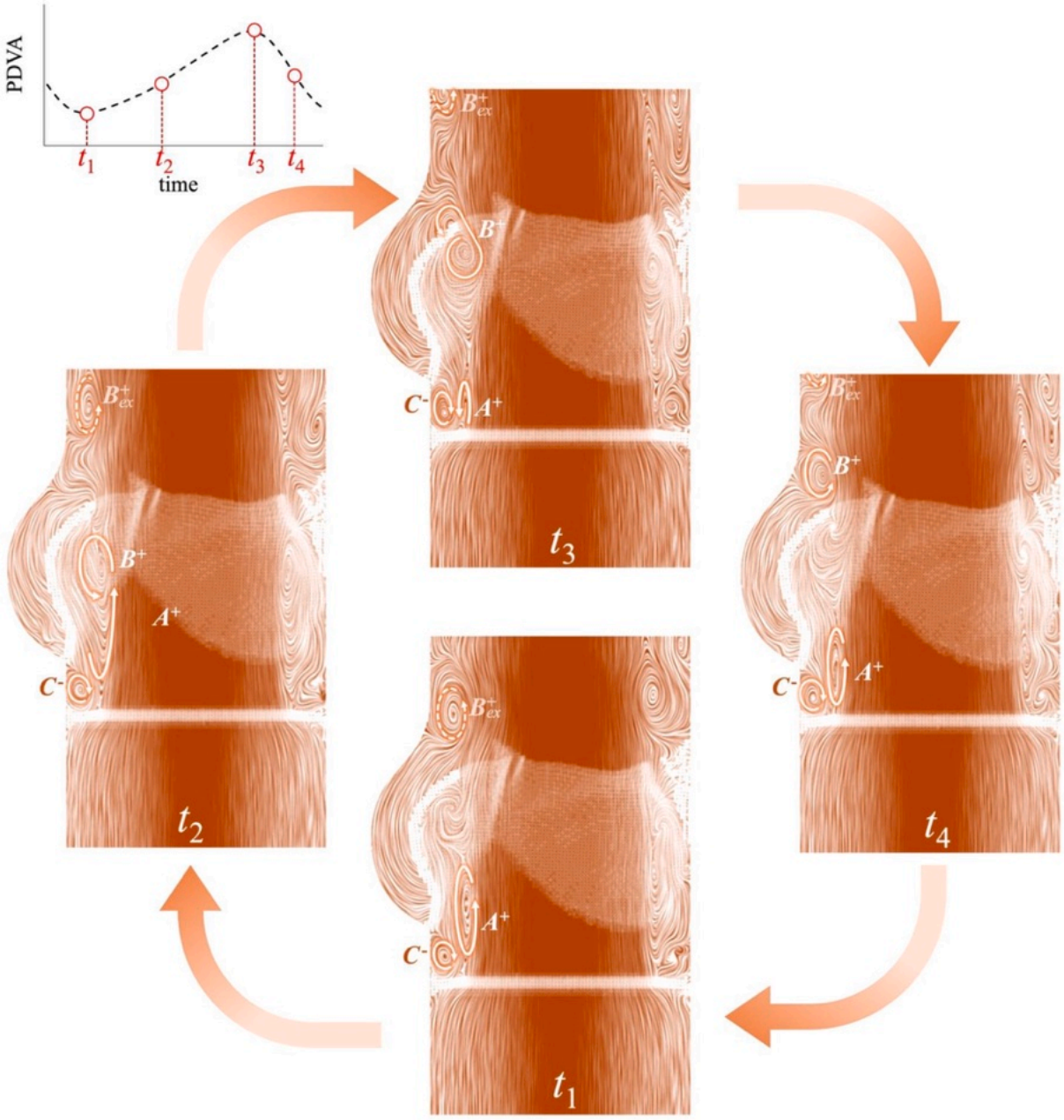

Fig. 7. Stiff SAM - velocity streamlines in a longitudinal cross-section at four characteristic instants of the fluttering cycle: t_1-trough corresponding to minimum PDVA (0.226 s); t_2-midline crossing during ascent (0.237 s); t_3-peak corresponding to maximum PDVA (0.248 s); t_4-midline crossing during descent (0.254 s).

vortical structures [49]. Despite the constant boundary pressure, the presence of the SAM induces a focalised central jet, which leads to a substantial increase in peak velocity with respect to the *healthy AV*, amounting to +41% and +74% for the *flexible* and *stiff SAM*s, respectively. This focalised central jet promotes the formation of vortical structures in the proximity of the leaflets and wall structures both in the presence of *flexible* and *stiff SAMs*. While in the case of the *flexible SAM* the membrane can deform under the effect of the flow, taking a funnel shape which expands its orifice and allows a smoother inlet of the flow, in the case of the *stiff SAMs* all effects appear amplified.

The alterations produced by the SAM are also evident in the vorticity (see Fig. 5b). The *healthy AV* exhibits a largely neutral vorticity region occupying most of the aortic root. Vorticity regions initiate at the LVOT wall and follow the internal leaflet profile, emerging from the leaflet free edge as trails that remain relatively straight along the aortic root. The gap between the leaflets and the Valsalva sinuses wall is interested by positive vorticity, suggesting the presence of some washout flow. In contrast, in the pathological cases the neutral zone is confined to the root axis and rotational flow develops, characterised by distinct negative and positive values (see *flexible SAM* and *stiff SAM*). The high vorticity trails arise from the membrane free edge, indicating that vortices sheding from the SAM dominate the downstream flow. These vortical structures travel to the outflow causing increased flow rotationality in the wake of the leaflet exit. Furthermore, the positive vorticity in the region between the leaflets and the Valsalva sinuses appears neutralised, and instead shifted into the concavity at the leaflets inflow side.

Potential blood damage was evaluated through shear stress analysis (see Fig. 5c). In the *healthy AV*, shear layers extend from the tip of the leaflets, whereas in the pathological scenarios these layers primarily develop from the membrane edge. It should be noted that the peak of shear stress observed in all cases keeps below 5 Pa, well below the haemolytic threshold identified by Leverett et al., which is in the range

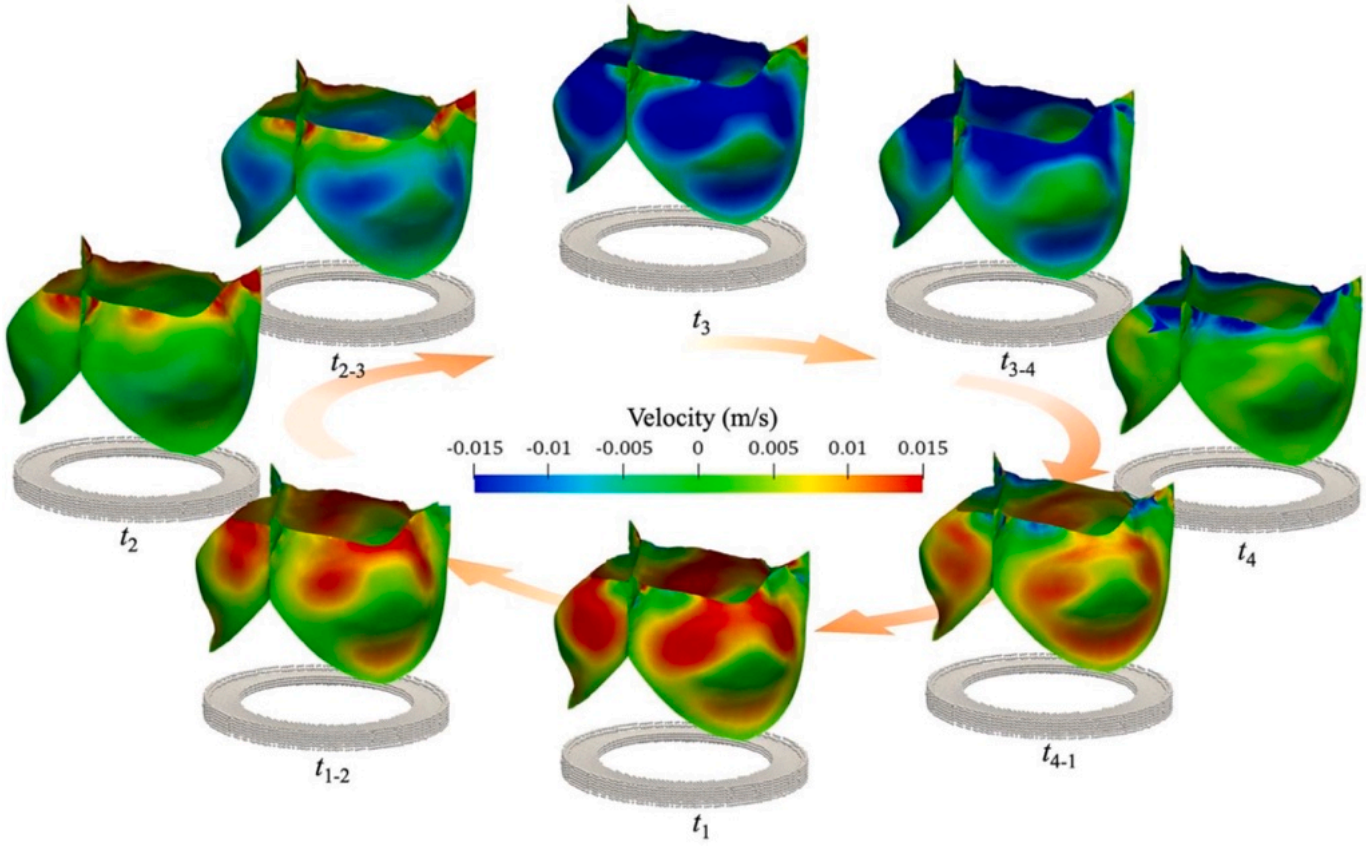

Fig. 8. Representation of the velocity fronts travelling the leaflet during the fluttering phenomenon in the presence of the stiff SAM.

of 150 Pa [76].

Clinical studies have reported leaflets fluttering in the presence of SAM, suggesting a driving role for the focused jet induced by the membrane impinging directly on the valve leaflets [15,27,28]. However, the mechanism identified in the present study is very different and directly related with fluid dynamic instabilities.

The presented model successfully achieves a steady configuration for the *healthy AV*, while the introduction of SAM resulted in fluttering. The mechanism underlying the phenomenon was investigated by analysing vortices dynamics through four key instants (t_1-t_4) of one PDVA oscillation cycle (see Figs. 6 and 7). The overall phenomenon is similar for the two types of membranes (*flexible SAM* in Fig. 6 and *stiff SAM* in Fig. 7), though with notable differences in vortex sizes and persistence. Specifically, the membrane sheds vortices whose dimension depends on the membrane flexibility.

In the case of the *flexible SAM* (see Fig. 6), at its outflow the membrane forms a near-wall counterflow of thickness comparable with the area occupied by the deformed membrane (see vortex tube A^+). From time t_1, this counterflow progressively extends toward the concavity at the inflow side of open leaflet, where by time t_2 evolves into a large positive vortex (indicated as B^+). This is subsequently advected downstream along the main flow direction. The presence of vortex B^+ exerts an outward (expanding) force on the leaflets, causing them to open further and thereby increasing the PDVA (see the PDVA oscillation cycle in Fig. 6). Eventually, at t_3, the leaflets are no longer able to confine vortex B^+, which escapes past their free edges and moves toward the valve outlet. This release relieves the load on the leaflets, and as a result the PDVA starts to decrease from t_3 (see the PDVA plot in Fig. 6), while vortex B^+ continues its progression into the ascending aorta (vortex B^+_{ex} at instants t_1 and t_2). During the phase of PDVA reduction, it is possible to observe a small negative counter-vortex ring (C^-) just above the membrane and adjacent to the LVOT wall. In the presence of *stiff SAM* (see Fig. 7), vortices have larger dimensions and persistence. Vortex B^+_{ex} is, in fact, visible for all the instants of the PDVA cycle, while it dissipates after time t_2 in the flexible SAM (see Fig. 6).

Fluttering induces alterations in the leaflets dynamics that, as suggested in the literature, may contribute to structural deterioration and the onset of aortic regurgitation [5,9,15,28]. Leaflets dynamics in the pathological configurations was investigated by analysing the velocity component normal to the leaflets surface. As shown in Fig. 8, this velocity exhibits marked variations throughout the PDVA cycle. These are symptoms of a complex local haemodynamics near the leaflet surface, associated with vortices and flow recirculation potentially supporting platelet aggregation and adhesion [36]. Leaflets undergo alternating positive and negative velocity fronts that cyclically form and advance from their belly to the free edge (see Fig. 8) leading to their abnormal motion. The velocity distribution and leaflets dynamics appears to be identical for the positive and negative events, with exception of the sign, confirming a symmetric bipolar oscillation typical of vortex shedding phenomena.

Mechanical shear stress plays a critical role in regulating valve extracellular matrix components [77,78] and may influence valvular physiology and pathology [79–81]. As shown Fig. 9, WSS magnitude and direction differ markedly between healthy and pathological conditions. In the *healthy AV* case, WSS is predominantly axially oriented and exhibits a well organised pattern (see Fig. 9a). In contrast, in the presence of the membrane, WSS distribution becomes highly irregular, with reduced axial dominance and comparable circumferential component. This effect is particularly visible on the aortic surface of the leaflet, where WSS magnitudes remain significantly lower than those of the healthy case. Such localised derangements in the mechanical environment may compromise structural integrity and influence calcification potentials. Although quantifying endothelial injury or inflammatory activation is beyond the scope of this study, the altered WSS

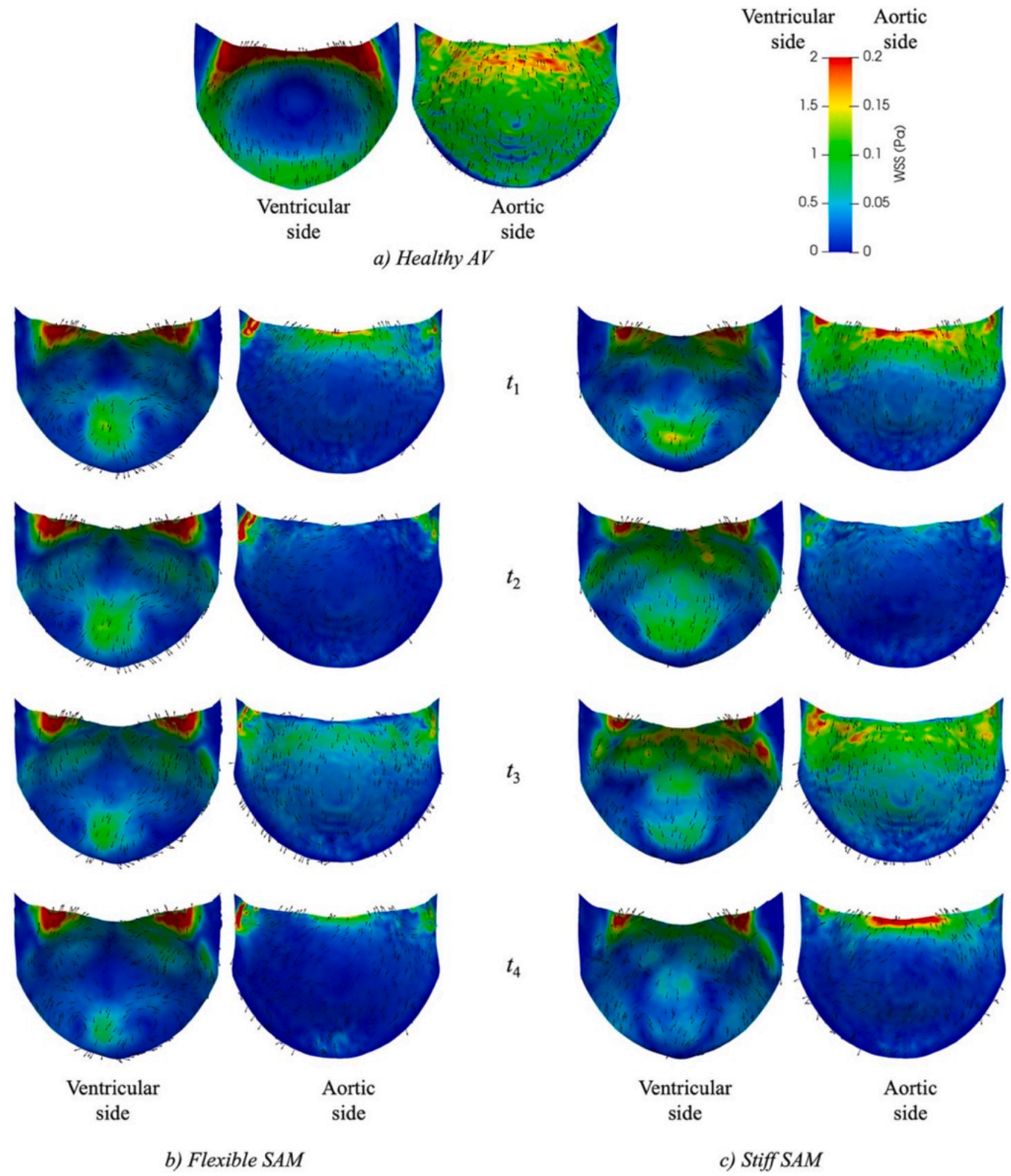

Fig. 9. Wall shear stress (WSS) contour map and vectors on the ventricular and aortic sides of one leaflet. a) Healthy AV; b) flexible SAM and c) stiff SAM.

distributions observed in the presence of the membrane indicate significant changes in the local mechanical environment. WSS represent a mechanical stimulus that, according to established literature, can influence the alignment and expression of endothelial cells and collagen, potentially compromising the valve integrity [36,50–52]. This is coherent with the higher incidence of lesions to the aortic valve reported in SAM patients which may cause aortic regurgitation, commonly attributed to the altered systolic jet [12,14]. This abnormal WSS might also induce a pro-inflammatory response on the fibrosa layer, ultimately leading to endothelial damage, calcification and increase in thrombogenicity [33,36,82].

5. Limitations

Some limitations and assumptions of this study should be highlighted.

Specifically, to better isolate the fluttering mechanisms and achieve a clear interpretation of the results, idealised geometries were used for the native leaflets, ascending aorta and subaortic membranes. Coronary arteries and their associated flows were not included in the model. Furthermore, the ventricular flow was highly idealised and modelled as a straight cylindrical conduit with uniform pressure. While this assumption does not capture the full three-dimensional flow complexity of the native left ventricle, it has been shown to be acceptable by previous more complex investigations [83]. Moreover, imposing spatially uniform pressure gradient at the aortic valve inlet is a common practice in the literature [62,84–86]. Nevertheless, patient-specific ventricular geometry and wall motion may influence local flow structures and should be considered in future studies aimed at clinical translation.

Although DSS lesions may manifest as either circumferential rings or incomplete crescent shape structures, in the present study an axisymmetric configuration was adopted to avoid introducing geometric complexities that might confound the interpretation of the fluttering mechanism. Future work will extend the analysis to more complex morphologies, such as asymmetric or crescent-shaped lesions.

Leaflets thickness was assumed constant, neglecting its variation in thickness, ranging from thinner regions in the belly to thicker areas at the free margin and nodulus [87].

Furthermore, also the material properties are highly simplified. Leaflets were approximated as linear elastic and isotropic, despite their non-linear anisotropic behaviour; however, this simplification has been shown not to alter substantially the results during valve opening, when the level of membrane strain is reduced [48,88].

The aortic root was assumed rigid, thereby neglecting vascular compliance and viscoelasticity. In the present framework, this assumption is considered acceptable due to the constant pressure loading, which is expected to produce negligible compliance-related effects. Nevertheless, future investigations addressing full cardiac cycle dynamics will require more advanced constitutive descriptions to account for aortic wall deformability.

Blood was modelled as an incompressible Newtonian fluid, a common assumption [35,36,43,48,89,90], demonstrated acceptable in studies involving large vessels and high shear rates [35,62,91]. Moreover, blood flow was modelled as laminar, coherently with several computational investigations of aortic valve haemodynamics [47,48,62,92,93], to reduce computational complexity and isolate the fundamental physical triggers of leaflet fluttering. This approach establishes a controlled and conservative baseline for the onset of the phenomenon, demonstrating that the oscillations originate from vortex shedding and flow–structure coupling, rather than from turbulence-induced instabilities. However, it does not account for the high Reynolds stress and turbulent fluctuations that may be present in severe DSS. Therefore, quantitative assessment of the turbulence-related haemolytic risk remains beyond the scope of the present work, and will require future investigations incorporating advanced turbulence modelling.

Finally, only the valve open phase was analysed, as the diastolic phase is inconsequential in assessing flutter [8,35]. This implies that the vortical structures associated with the valve opening and closure dynamics, as well as diastolic washout flows, were not modelled. This assumption is further supported by experimental tests conducted under similar conditions [8]. While the present study isolates the fluttering mechanism, the inherent pulsatility of the cardiac cycle undoubtedly influences both the fluid shear stress and leaflet behaviour. Future research will therefore aim to evaluate the impact of fluttering across the whole cardiac cycle.

6. Conclusions

This study investigates the complex haemodynamic alterations induced by discrete subaortic stenosis by means of FSI numerical analysis. To this aim, a mono-physics FSI approach was employed, handling the direct interaction between the blood flow and the leaflets and membrane structures, without the need to define interfaces between the fluid and solid phases.

Particular attention was given to the leaflet fluttering mechanism, a complex and clinically relevant phenomenon associated with blood damage, regurgitation, early calcification and fatigue failure. Two types of membranes, discrete thin SAM layer and thick fibromuscular ridge SAM, were analysed and compared with an equivalent healthy aortic valve model.

Both pathological cases exhibited significant PDVA oscillations, absent in the healthy configuration. The stiff fibromuscular ridge SAM produced much larger amplitude and higher frequency compared with the thin SAM.

Analysis of blood velocity, vorticity and shear stress provided critical insights into the origin of fluttering, revealing that this is caused by vortices periodically shed from the membrane edge, acting on the leaflets while travelling downstream. These were significantly larger, more defined and generated at higher frequency for the *stiff SAM* model. Although peak shear stresses remained below the haemolytic threshold, flow recirculation and vortex trapping may promote platelet aggregation.

Leaflet kinematic was characterised by cyclic travelling waves of positive and negative normal velocity, highlighting the strong coupling between local flow patterns and leaflet dynamics.

Furthermore, abnormal WSS distribution observed in the presence of the membrane may contribute to adverse remodelling of the valve extracellular matrix and to endothelial damage.

Overall, this computational framework provides a powerful non-invasive tool for elucidating the mechanisms underlying leaflet flutter and its haemodynamic consequences, with potential implications for clinical risk stratification and treatment planning.

CRediT authorship contribution statement

Alessandra Monteleone: Writing – original draft, Visualization, Validation, Software, Resources, Methodology, Investigation, Formal analysis, Data curation, Conceptualization. **Gaetano Burriesci:** Writing – review & editing, Visualization, Validation, Supervision, Resources, Project administration, Methodology, Investigation, Formal analysis, Data curation, Conceptualization.

Ethics statement

Not applicable.

Declaration of competing interest

The authors declare that they have no known competing financial interests or personal relationships that could have appeared to influence the work reported in this paper.

Appendix A. Supplementary data

Supplementary data related to this article can be found at https://doi.org/10.1016/j.compbiomed.2026.111645.

References

[1] D.D. Massé, J.A. Shar, K.N. Brown, S.G. Keswani, K.J. Grande-Allen, P. Sucosky, Discrete subaortic stenosis: perspective roadmap to a complex disease, Front. Cardiovasc. Med. 5 (2018), https://doi.org/10.3389/fcvm.2018.00122.

[2] T. Asif, L.A. Georger, K. Sardesai, M. Kosinska, M.S. Miran, Challenges of management of subaortic membrane in a young adult patient: a case report, Cureus (2023), https://doi.org/10.7759/cureus.48571.
[3] T. Hatab, S. Zaid, S. Toro, P. Wessly, M. Malahfji, N. Faza, S.H. Little, N.S. Kleiman, M.J. Reardon, S.S. Goel, Now you see me now you don't, JACC Case Rep. 18 (2023) 101916, https://doi.org/10.1016/j.jaccas.2023.101916.
[4] L. Ku, X. Ma, A subaortic membrane causing left ventricular outflow tract obstruction, Radiology 310 (2024), https://doi.org/10.1148/radiol.232805.
[5] J. Aboulhosn, J.S. Child, Left ventricular outflow obstruction, Circulation 114 (2006) 2412–2422, https://doi.org/10.1161/CIRCULATIONAHA.105.592089.
[6] J. Dong, Z. Li, Y. Sun, C. Du, S. Liu, K. Yang, X. Pan, S. Dong, The fate of aortic valve after surgical repair for discrete membranous subaortic stenosis in pediatric patients, J. Thorac. Cardiovasc. Surg. (2025), https://doi.org/10.1016/j.jtcvs.2025.05.013.
[7] K.K. Ozsin, F. Toktas, U.S. Sanri, S. Yavuz, Discrete subaortic stenosis in an adult patient, The European Research Journal 2 (2016) 66, https://doi.org/10.18621/eurj.2016.2.1.66.
[8] S. Di Leonardo, D. Vella, C. Pisano, V. Argano, G. Burriesci, Hydrodynamic alterations produced by subaortic membranes: an in vitro study, IRBM 46 (2025) 100897, https://doi.org/10.1016/j.irbm.2025.100897.
[9] M. Sandstedt, M. Sandstedt, J. Gudnason, M. Börjesson, F. Dangardt, J. Sunnegårdh, Subvalvular membranous aortic stenosis in Swedish children, a retrospective cohort study between 1994 and 2019, cardiol, Young 35 (2025) 1161–1171, https://doi.org/10.1017/S1047951125001854.
[10] Y. Perez, J.A. Dearani, W.R. Miranda, E.H. Stephens, Subaortic stenosis in adult patients with atrioventricular septal defect, Ann. Thorac. Surg. 115 (2023) 479–484, https://doi.org/10.1016/j.athoracsur.2022.08.011.
[11] S.R. Devabhaktuni, E. Chakfeh, A.O. Malik, J.A. Pengson, J. Rana, C.H. Ahsan, Subvalvular aortic stenosis: a review of current literature, Clin. Cardiol. 41 (2018) 131–136, https://doi.org/10.1002/clc.22775.
[12] J.M. Oliver, A. González, P. Gallego, A. Sánchez-Recalde, F. Benito, J.M. Mesa, Discrete subaortic stenosis in adults: increased prevalence and slow rate of progression of the obstruction and aortic regurgitation, J. Am. Coll. Cardiol. 38 (2001) 835–842, https://doi.org/10.1016/S0735-1097(01)01464-4.
[13] E.A. Newfeld, A.J. Muster, M.H. Paul, F.S. Idriss, W.L. Riker, Discrete subvalvular aortic stenosis in childhood, Am. J. Cardiol. 38 (1976) 53–61, https://doi.org/10.1016/0002-9149(76)90062-X.
[14] D.T. Kelly, E. Wulfsberc, R.D. Rowe, Discrete subaortic stenosis, Circulation 46 (1972) 309–322, https://doi.org/10.1161/01.CIR.46.2.309.
[15] S.S. Rana, M.G. Kumar, G.D. Puri, I. Biswas, Subaortic membrane in adult mimicking rheumatic combined aortic stenosis and regurgitation: role of transesophageal echocardiography in accurate diagnosis, J. Perioperat. Echocardiogr. 6 (2018) 44–47, https://doi.org/10.5005/jp-journals-10034-1088.
[16] P. Ji, S. Brimmer, J.S. Heinle, J. Grande-Allen, R.K. Birla, S.G. Keswani, Development of a novel *In Vitro* Co-culture system for discrete subaortic stenosis, AIMS Bioeng. 12 (2025) 357–369, https://doi.org/10.3934/bioeng.2025016.
[17] J.A. Shar, K.N. Brown, S.G. Keswani, J. Grande-Allen, P. Sucosky, Impact of aortoseptal angle abnormalities and discrete subaortic stenosis on left-ventricular outflow tract hemodynamics: preliminary computational assessment, Front. Bioeng. Biotechnol. 8 (2020), https://doi.org/10.3389/fbioe.2020.00114.
[18] S.H. Fatimi, U. Ahmad, M.A. Javed, S. Shamim, R. Ahmad, Familial membranous subaortic stenosis: review of familial inheritance patterns and a case report, J. Thorac. Cardiovasc. Surg. 132 (2006) 1484–1486.e1, https://doi.org/10.1016/j.jtcvs.2006.08.034.
[19] J.E. Foker, Outcomes and questions about discrete subaortic stenosis, Circulation 127 (2013) 1447–1450, https://doi.org/10.1161/CIRCULATIONAHA.113.001619.
[20] L.A. Barboza, F. de M. Garcia, J. Barnoya, J.R. Leon-Wyss, A.R. Castañeda, Subaortic membrane and aorto-septal angle, World J. Pediatr. Congenit. Heart Surg. 4 (2013) 253–261, https://doi.org/10.1177/2150135113485760.
[21] J.A. Shar, S.G. Keswani, K.J. Grande-Allen, P. Sucosky, Significance of aortoseptal angle anomalies to left ventricular hemodynamics and subaortic stenosis: a numerical study, Comput. Biol. Med. 146 (2022) 105613, https://doi.org/10.1016/j.compbiomed.2022.105613.
[22] C.A. Warnes, R.G. Williams, T.M. Bashore, J.S. Child, H.M. Connolly, J.A. Dearani, P. del Nido, J.W. Fasules, T.P. Graham, Z.M. Hijazi, S.A. Hunt, M.E. King, M. J. Landzberg, P.D. Miner, M.J. Radford, E.P. Walsh, G.D. Webb, ACC/AHA 2008 guidelines for the management of adults with congenital heart disease, J. Am. Coll. Cardiol. 52 (2008) e143–e263, https://doi.org/10.1016/j.jacc.2008.10.001.
[23] D. van der Linde, J.W. Roos-Hesselink, D. Rizopoulos, H.J. Heuvelman, W. Budts, A.P.J. van Dijk, M. Witsenburg, S.C. Yap, A. Oxenius, C.K. Silversides, E. N. Oechslin, A.J.J.C. Bogers, J.J.M. Takkenberg, Surgical outcome of discrete subaortic stenosis in adults, Circulation 127 (2013) 1184–1191, https://doi.org/10.1161/CIRCULATIONAHA.112.000883.
[24] D.S. Ezon, Fixed subaortic stenosis: a clinical dilemma for Clinicians and patients, congenit, Heart Dis. (2013), https://doi.org/10.1111/chd.12127 n/a-n/a.
[25] M. Marasini, L. Zannini, G.P. Ussia, R. Pinto, R. Moretti, F. Lerzo, G. Pongiglione, Discrete subaortic stenosis: incidence, morphology and surgical impact of associated subaortic anomalies, Ann. Thorac. Surg. 75 (2003) 1763–1768, https://doi.org/10.1016/S0003-4975(02)05027-0.
[26] E. Buratto, I.E. Konstantinov, Commentary: subaortic membrane: not as simple as it seems, J. Thorac. Cardiovasc. Surg. (2025), https://doi.org/10.1016/j.jtcvs.2025.06.018.
[27] R.H. Davis, H. Feigenbaum, S. Chang, L.L. Konecke, J.C. Dillon, Echocardiographic manifestations of discrete subaortic stenosis, Am. J. Cardiol. 33 (1974) 277–280, https://doi.org/10.1016/0002-9149(74)90289-6.
[28] V. Itare, N. Javed, R.P. Rivas, N. Mandalapu, A. Mehta, N. Ali, S. Ashraf, M. Molina, M. Nicu, Subaortic membrane in adult patients: retrospective study of clinical characteristics, outcomes, and echocardiographic associations and review of literature, Int. J. Cardiovasc. Imag. 41 (2025) 1797–1810, https://doi.org/10.1007/s10554-025-03489-5.
[29] E.L. Johnson, M.C.H. Wu, F. Xu, N.M. Wiese, M.R. Rajanna, A.J. Herrema, B. Ganapathysubramanian, T.J.R. Hughes, M.S. Sacks, M.-C. Hsu, Thinner biological tissues induce leaflet flutter in aortic heart valve replacements, Proc. Natl. Acad. Sci. 117 (2020) 19007–19016, https://doi.org/10.1073/pnas.2002821117.
[30] J.H. Lee, L.N. Scotten, R. Hunt, T.G. Caranasos, J.P. Vavalle, B.E. Griffith, Bioprosthetic aortic valve diameter and thickness are directly related to leaflet fluttering: results from a combined experimental and computational modeling study, JTCVS Open 6 (2021) 60–81, https://doi.org/10.1016/j.xjon.2020.09.002.
[31] D. Obrist, T.P. Carrel, Commentary: leaflet fluttering of bioprosthetic valve—Does it matter? JTCVS Open 6 (2021) 82–83, https://doi.org/10.1016/j.xjon.2020.10.009.
[32] A.H. de F. Avelar, J.A. Canestri, C. Bim, M.G.M. Silva, R. Huebner, M. Pinotti, Quantification and analysis of leaflet flutter on biological prosthetic cardiac valves, Artif. Organs 41 (2017) 835–844, https://doi.org/10.1111/aor.12856.
[33] L. Chen, Z. Zhang, T. Li, Y. Chen, A review of biomechanical studies of heart valve flutter, Fluid 9 (2024) 254, https://doi.org/10.3390/fluids9110254.
[34] J.H. Lee, A.D. Rygg, E.M. Kolahdouz, S. Rossi, S.M. Retta, N. Duraiswamy, L. N. Scotten, B.A. Craven, B.E. Griffith, Fluid–structure interaction models of bioprosthetic heart valve dynamics in an experimental pulse duplicator, Ann. Biomed. Eng. 48 (2020) 1475–1490, https://doi.org/10.1007/s10439-020-02466-4.
[35] M.C.B. Costa, S. de F. Gonçalves, J.V.C. Fleury, M.L.F. da Silva, R. Huebner, A.H. de F. Avelar, Computational fluid–structure analysis of the impact of leaflet thickness and protrusion height on the flutter phenomenon in aortic valve bioprostheses, Meccanica 59 (2024) 685–701, https://doi.org/10.1007/s11012-024-01809-y.
[36] M.C.B. Costa, S. de F. Gonçalves, M.L.F. da Silva, J.V.C. Fleury, R. Huebner, A.H. de F. Avelar, The influence of leaflet flutter of the aortic valve bioprostheses on leaflet calcification and endothelial activation, Comput. Biol. Med. 187 (2025) 109765, https://doi.org/10.1016/j.compbiomed.2025.109765.
[37] B. Vennemann, T. Rösgen, P.P. Heinisch, D. Obrist, Leaflet kinematics of mechanical and bioprosthetic aortic valve prostheses, ASAIO J. 64 (2018) 651–661, https://doi.org/10.1097/MAT.0000000000000687.
[38] Y. Zhu, M.H. Park, P.K. Pandya, C.J. Stark, D.M. Mullis, S.K. Walsh, J.Y. Kim, C. A. Wu, B.M. Baccouche, S.H. Lee, A.S. Baraka, H. Joo, S. Yajima, S. Elde, Y.J. Woo, Biomechanics and clinical outcomes of various conduit configurations in valve sparing aortic root replacement, Ann. Cardiothorac. Surg. 12 (2023) 326–337, https://doi.org/10.21037/acs-2023-avs2-0068.
[39] X. Liu, A. Lee, Y. Wang, T.P. Hoang, K.S. Yee, L. Mosse, N. Karajan, D.S. Winlaw, S. Naficy, D.F. Fletcher, Fluid-structure interaction analysis of bioinspired polymeric heart valves with experimental validation, Comput. Methods Progr. Biomed. 268 (2025) 108839, https://doi.org/10.1016/j.cmpb.2025.108839.
[40] A. Monteleone, A. Viola, E. Napoli, G. Burriesci, Modelling of thrombus formation using smoothed particle hydrodynamics method, PLoS One 18 (2023) e0281424, https://doi.org/10.1371/journal.pone.0281424.
[41] A.M. Lo Presti, A. Monteleone, G. Musotto, A. Tamburini, E. Napoli, G. Burriesci, Modelling of thrombus formation, growth and embolisation in the left atrial appendage under atrial fibrillation, Comput. Biol. Med. 191 (2025) 110134, https://doi.org/10.1016/j.compbiomed.2025.110134.
[42] A.M. Tango, J. Salmonsmith, A. Ducci, G. Burriesci, Validation and extension of a fluid–structure interaction model of the healthy aortic valve, Cardiovasc. Eng. Technol. 9 (2018) 739–751, https://doi.org/10.1007/s13239-018-00391-1.
[43] J. De Hart, G.W.M. Peters, P.J.G. Schreurs, F.P.T. Baaijens, A three-dimensional computational analysis of fluid–structure interaction in the aortic valve, J. Biomech. 36 (2003) 103–112, https://doi.org/10.1016/S0021-9290(02)00244-0.
[44] A. Laadhari, G. Székely, Eulerian finite element method for the numerical modeling of fluid dynamics of natural and pathological aortic valves, J. Comput. Appl. Math. 319 (2017) 236–261, https://doi.org/10.1016/j.cam.2016.11.042.
[45] A.M. Tango, A. Ducci, G. Burriesci, In silico study of the ageing effect upon aortic valves, J. Fluid Struct. 103 (2021) 103258, https://doi.org/10.1016/j.jfluidstructs.2021.103258.
[46] A. Chen, A. Azriff Basri, N. Bin Ismail, K. Arifin Ahmad, Hemodynamic effects of subaortic stenosis on blood flow characteristics of a mechanical heart valve based on OpenFOAM simulation, Bioengineering 10 (2023) 312, https://doi.org/10.3390/bioengineering10030312.
[47] C. Guivier, V. Deplano, P. Pibarot, New insights into the assessment of the prosthetic valve performance in the presence of subaortic stenosis through a fluid–structure interaction model, J. Biomech. 40 (2007) 2283–2290, https://doi.org/10.1016/j.jbiomech.2006.10.010.
[48] J.A. Shar, S.G. Keswani, K.J. Grande-Allen, P. Sucosky, Computational assessment of valvular dysfunction in discrete subaortic stenosis: a parametric study, Cardiovasc. Eng. Technol. 12 (2021) 559–575, https://doi.org/10.1007/s13239-020-00513-8.
[49] A. Monteleone, S. Di Leonardo, E. Napoli, G. Burriesci, A novel mono-physics particle-based approach for the simulation of cardiovascular fluid-structure interaction problems, Comput. Methods Progr. Biomed. 245 (2024) 108034, https://doi.org/10.1016/j.cmpb.2024.108034.
[50] E. Tsolaki, P. Corso, R. Zboray, J. Avaro, C. Appel, M. Liebi, S. Bertazzo, P. P. Heinisch, T. Carrel, D. Obrist, I.K. Herrmann, Multiscale multimodal characterization and simulation of structural alterations in failed bioprosthetic

heart valves, Acta Biomater. 169 (2023) 138–154, https://doi.org/10.1016/j.actbio.2023.07.044.
[51] L. Ge, F. Sotiropoulos, Direction and magnitude of blood flow shear stresses on the leaflets of aortic valves: is there a link with valve calcification? J. Biomech. Eng. 132 (2010) https://doi.org/10.1115/1.4000162.
[52] A. Arzani, S.C. Shadden, Wall shear stress fixed points in cardiovascular fluid mechanics, J. Biomech. 73 (2018) 145–152, https://doi.org/10.1016/j.jbiomech.2018.03.034.
[53] E. Napoli, M. De Marchis, E. Vitanza, PANORMUS-SPH. A new smoothed particle hydrodynamics solver for incompressible flows, Comput. Fluids 106 (2015) 185–195, https://doi.org/10.1016/j.compfluid.2014.09.045.
[54] L.B. Lucy, A numerical approach to the testing of the fission hypothesis, Astron. J. 82 (1977) 1013, https://doi.org/10.1086/112164.
[55] R.A. Gingold, J.J. Monaghan, Smoothed particle hydrodynamics: theory and application to non-spherical stars, Mon. Not. Roy. Astron. Soc. 181 (1977) 375–389, https://doi.org/10.1093/mnras/181.3.375.
[56] M.B. Liu, G.R. Liu, Smoothed particle hydrodynamics (SPH): an overview and recent developments, Arch. Comput. Methods Eng. 17 (2010) 25–76, https://doi.org/10.1007/s11831-010-9040-7.
[57] J.J. Monaghan, Smoothed particle hydrodynamics and its diverse applications, Annu. Rev. Fluid Mech. 44 (2012) 323–346, https://doi.org/10.1146/annurev-fluid-120710-101220.
[58] G. Marom, Numerical methods for fluid–structure interaction models of aortic valves, Arch. Comput. Methods Eng. 22 (2015) 595–620, https://doi.org/10.1007/s11831-014-9133-9.
[59] A.M. Bavo, G. Rocatello, F. Iannaccone, J. Degroote, J. Vierendeels, P. Segers, Fluid-structure interaction simulation of prosthetic aortic valves: Comparison between immersed boundary and arbitrary lagrangian-eulerian techniques for the mesh representation, PLoS One 11 (2016) e0154517, https://doi.org/10.1371/journal.pone.0154517.
[60] T.E. Tezduyar, S. Sathe, Modelling of fluid–structure interactions with the space–time finite elements: solution techniques, Int. J. Numer. Methods Fluid. 54 (2007) 855–900, https://doi.org/10.1002/fld.1430.
[61] J. Sigüenza, D. Pott, S. Mendez, S.J. Sonntag, T.A.S. Kaufmann, U. Steinseifer, F. Nicoud, Fluid-structure interaction of a pulsatile flow with an aortic valve model: a combined experimental and numerical study, Int. J. Numer. Methods Biomed. Eng. 34 (2018), https://doi.org/10.1002/cnm.2945.
[62] A.M. Tango, A. Monteleone, A. Ducci, G. Burriesci, Analysis of the haemodynamic changes caused by surgical and transcatheter aortic valve replacements by means fluid-structure interaction simulations, Comput. Biol. Med. 186 (2025) 109673, https://doi.org/10.1016/j.compbiomed.2025.109673.
[63] M. Thubrikar, The Aortic Valve, 1990. Boca Raton.
[64] W.M. Swanson, R.E. Clark, Dimensions and geometric relationships of the human aortic value as a function of pressure, Circ. Res. 35 (1974) 871–882, https://doi.org/10.1161/01.RES.35.6.871.
[65] H. Reul, A. Vahlbruch, M. Giersiepen, Th Schmitz-Rode, V. Hirtz, S. Effert, The geometry of the aortic root in health, at valve disease and after valve replacement, J. Biomech. 23 (1990) 181–191, https://doi.org/10.1016/0021-9290(90)90351-3.
[66] M. Motro, A. Schneeweiss, A. Shem-Tov, P. Benjamin, E. Kaplinsky, J. Hegesh, Correlation of distance from subaortic membrane to base of the right aortic valve cusp and the development of aortic regurgitation in mild discrete subaortic stenosis, Am. J. Cardiol. 64 (1989) 395–396, https://doi.org/10.1016/0002-9149(89)90544-4.
[67] A. Monteleone, M. Monteforte, E. Napoli, Inflow/outflow pressure boundary conditions for smoothed particle hydrodynamics simulations of incompressible flows, Comput. Fluids 159 (2017) 9–22, https://doi.org/10.1016/j.compfluid.2017.09.011.
[68] R. Toninato, J. Salmon, F.M. Susin, A. Ducci, G. Burriesci, Physiological vortices in the sinuses of Valsalva: an in vitro approach for bio-prosthetic valves, J. Biomech. 49 (2016), https://doi.org/10.1016/j.jbiomech.2016.05.027.
[69] Y.C. Fung, S.C. Cowin, Biomechanics: mechanical properties of living tissues, in: second ed.J. Appl. Mech., vol. 61, 1994, https://doi.org/10.1115/1.2901550, 1007–1007.
[70] F.J. Schoen, R.J. Levy, Tissue heart valves: current challenges and future research perspectives, J. Biomed. Mater. Res. 47 (1999) 439–465, https://doi.org/10.1002/(SICI)1097-4636(19991215)47:4<439::AID-JBM1>3.0.CO;2-O.
[71] M. Misfeld, H.-H. Sievers, Heart valve macro- and microstructure, Phil. Trans. Biol. Sci. 362 (2007) 1421–1436, https://doi.org/10.1098/rstb.2007.2125.
[72] A. Hasan, K. Ragaert, W. Swieszkowski, Š. Selimović, A. Paul, G. Camci-Unal, M.R. K. Mofrad, A. Khademhosseini, Biomechanical properties of native and tissue engineered heart valve constructs, J. Biomech. 47 (2014) 1949–1963, https://doi.org/10.1016/j.jbiomech.2013.09.023.
[73] D. Mavrilas, Y. Missirlis, An approach to the optimization of preparation of bioprosthetic heart valves, J. Biomech. 24 (1991) 331–339, https://doi.org/10.1016/0021-9290(91)90351-M.
[74] S. Bozkurt, G.L.G.L. Preston-Maher, R. Torii, G. Burriesci, Design, analysis and testing of a novel mitral valve for transcatheter implantation, Ann. Biomed. Eng. 45 (2017), https://doi.org/10.1007/s10439-017-1828-2.
[75] L.N. Scotten, D.K. Walker, New laboratory technique measures projected dynamic area of prosthetic heart valves, J. Heart Valve Dis. 13 (2004) 120–132. ; discussion 132-3.
[76] L.B. Leverett, J.D. Hellums, C.P. Alfrey, E.C. Lynch, Red blood cell damage by shear stress, Biophys. J. 12 (1972) 257–273, https://doi.org/10.1016/S0006-3495(72)86085-5.
[77] N. Mongkoldhumrongkul, N. Latif, M.H. Yacoub, A.H. Chester, Effect of side-specific valvular shear stress on the content of extracellular matrix in aortic valves, Cardiovasc. Eng. Technol. 9 (2018) 151–157, https://doi.org/10.1007/s13239-016-0280-z.
[78] A. Gasté, D. Marchese, A. Faucherre, L. Lopez, E. Bertrand, A. Théron, M. Herbane, A. Seddik, C. Jopling, J.-F. Avierinos, H. Ait-Oufella, V. Deplano, S. Zaffran, EGFR-mediated mechanotransduction in aortic valve cells: a key pathway in response to wall shear stress. https://doi.org/10.1101/2025.03.10.642402, 2025.
[79] M.S. Sacks, A.P. Yoganathan, Heart valve function: a biomechanical perspective, Phil. Trans. Biol. Sci. 362 (2007) 1369–1391, https://doi.org/10.1098/rstb.2007.2122.
[80] K.D. O'Brien, Pathogenesis of calcific aortic valve disease, Arterioscler. Thromb. Vasc. Biol. 26 (2006) 1721–1728, https://doi.org/10.1161/01.ATV.0000227513.13697.ac.
[81] V. Gupta, K. Grandeallen, Effects of static and cyclic loading in regulating extracellular matrix synthesis by cardiovascular cells, Cardiovasc. Res. 72 (2006) 375–383, https://doi.org/10.1016/j.cardiores.2006.08.017.
[82] D. Hoehn, L. Sun, P. Sucosky, Role of pathologic shear stress alterations in aortic valve endothelial activation, Cardiovasc. Eng. Technol. 1 (2010) 165–178, https://doi.org/10.1007/s13239-010-0015-5.
[83] C.J. Carmody, G. Burriesci, I.C. Howard, E.A. Patterson, An approach to the simulation of fluid–structure interaction in the aortic valve, J. Biomech. 39 (2006) 158–169, https://doi.org/10.1016/j.jbiomech.2004.10.038.
[84] F. Sturla, E. Votta, M. Stevanella, C.A. Conti, A. Redaelli, Impact of modeling fluid–structure interaction in the computational analysis of aortic root biomechanics, Med. Eng. Phys. 35 (2013) 1721–1730, https://doi.org/10.1016/j.medengphy.2013.07.015.
[85] G. Marom, R. Haj-Ali, E. Raanani, H.-J. Schäfers, M. Rosenfeld, A fluid–structure interaction model of the aortic valve with coaptation and compliant aortic root, Med. Biol. Eng. Comput. 50 (2012) 173–182, https://doi.org/10.1007/s11517-011-0849-5.
[86] G.B. Kalyana Sundaram, K.R. Balakrishnan, R.K. Kumar, Aortic valve dynamics using a fluid structure interaction model – the physiology of opening and closing, J. Biomech. 48 (2015) 1737–1744, https://doi.org/10.1016/j.jbiomech.2015.05.012.
[87] K.J. Grande, R.P. Cochran, P.G. Reinhall, K.S. Kunzelman, Stress variations in the human aortic root and valve: the role of anatomic asymmetry, Ann. Biomed. Eng. 26 (1998) 534–545, https://doi.org/10.1114/1.122.
[88] D. Wiltz, C. Alexander, R. L, A.A. Blancas, M. C, X. Zhang, K. Jane, Extracellular matrix organization, structure, and function, in: Calcific Aortic Valve Disease, InTech, 2013, https://doi.org/10.5772/52842.
[89] W. Mao, A. Caballero, R. McKay, C. Primiano, W. Sun, Fully-coupled fluid-structure interaction simulation of the aortic and mitral valves in a realistic 3D left ventricle model, PLoS One 12 (2017) e0184729, https://doi.org/10.1371/journal.pone.0184729.
[90] R. van Loon, P.D. Anderson, F.N. van de Vosse, A fluid–structure interaction method with solid-rigid contact for heart valve dynamics, J. Comput. Phys. 217 (2006) 806–823, https://doi.org/10.1016/j.jcp.2006.01.032.
[91] I. Borazjani, Fluid–structure interaction, immersed boundary-finite element method simulations of bio-prosthetic heart valves, Comput. Methods Appl. Mech. Eng. 257 (2013) 103–116, https://doi.org/10.1016/j.cma.2013.01.010.
[92] K. Cao, M. BukaČ, P. Sucosky, Three-dimensional macro-scale assessment of regional and temporal wall shear stress characteristics on aortic valve leaflets, Comput. Methods Biomech. Biomed. Eng. 19 (2016) 603–613, https://doi.org/10.1080/10255842.2015.1052419.
[93] S. Annerel, J. Degroote, T. Claessens, P. Segers, P. Verdonck, J. Vierendeels, The upstream boundary condition influences the leaflet opening dynamics in the numerical FSI simulation of an aortic BMHV, Int. J. Numer. Methods Biomed. Eng. 28 (2012) 745–760, https://doi.org/10.1002/cnm.2470.